

# Three-dimensional fast elemental mapping by soft X-ray dual-energy focal stacks imaging

Limei Ma,<sup>a</sup> Zijian Xu,<sup>a</sup> Zhi Guo,<sup>a</sup> Benjamin Watts,<sup>b</sup> Jinyou Lin,<sup>a\*</sup> Xiangzhi Zhang<sup>a\*</sup> and Renzhong Tai<sup>a\*</sup>

<sup>a</sup>Shanghai Synchrotron Radiation Facility, Shanghai Advanced Research Institute, Chinese Academy of Sciences, Shanghai 201204, People's Republic of China, and <sup>b</sup>Swiss Light Source, Paul Scherrer Institute, 5232 Villigen, Switzerland. \*Correspondence e-mail: linjinyou@zjlab.org.cn, zhangxiangzhi@zjlab.org.cn, tairenzhong@zjlab.org.cn

Received 15 December 2020

Accepted 18 March 2021

Edited by A. Momose, Tohoku University, Japan

**Keywords:** 3D elemental distinguishing; dual-energy focal stacks imaging method; X-ray microscopy; STXM.

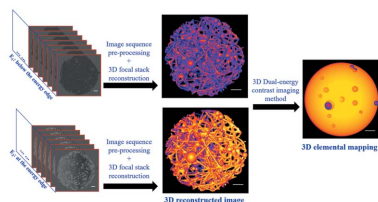
**Supporting information:** this article has supporting information at journals.iucr.org/s

The three-dimensional (3D) dual-energy focal stacks (FS) imaging method has been developed to quickly obtain the spatial distribution of an element of interest in a sample; it is a combination of the 3D FS imaging method and two-dimensional (2D) dual-energy contrast imaging based on scanning transmission soft X-ray microscopy (STXM). A simulation was firstly performed to verify the feasibility of the 3D elemental reconstruction method. Then, a sample of composite nanofibers, polystyrene doped with ferric acetylacetonate [Fe(acac)<sub>3</sub>], was further investigated to quickly reveal the spatial distribution of Fe(acac)<sub>3</sub> in the sample. Furthermore, the data acquisition time was less than that for STXM nanotomography under similar resolution conditions and did not require any complicated sample preparation. The novel approach of 3D dual-energy FS imaging, which allows fast 3D elemental mapping, is expected to provide invaluable information for biomedicine and materials science.

## 1. Introduction

Porous electrospun nanofibers, as superior one-dimensional nanostructures, have been applied in many fields such as electrochemical anodization, catalysis, absorption, *etc.* (González del Campo *et al.*, 2018; Zhang, Han *et al.*, 2010; Jo *et al.*, 2018). Recent works on electrospun nanofibers have dealt with the incorporation of different types of inorganic nanoparticles into this material for diverse functions (Lin, Shang *et al.*, 2012; Miyamoto *et al.*, 2017). Iron acetylacetonate [Fe(acac)<sub>3</sub>, acetylacetonate(acac)] dispersed into polymer nanofibers make it attractive in magnetic devices and biomagnetic regimes (Mahapatra *et al.*, 2013; Moatmed *et al.*, 2019). Therefore, investigating composite nanofibers decorated with Fe(acac)<sub>3</sub> provides potential value in biomaterials and nanoscience.

Traditionally, nanoscale investigation of the internal structure within nanofibers has been possible using various techniques including soft X-ray and electron microscopies, which are limited to investigations of thin samples (Shenhar & Rotello, 2003; Lin, Ding *et al.*, 2012). For example, in transmission electron microscopy, sample preparation and mechanical slicing procedures are essential for thick samples, and scanning electron microscopy only enables surface or cross-section microstructures to be observed (McIntosh *et al.*, 2005; Wei *et al.*, 2017). Typically, nanotomography is the commonly used technique for the three-dimensional (3D) imaging-based scanning transmission soft X-ray microscope (STXM), which is still a challenge for thick, large size samples due to high absorption for rotation at large angles (Johansson *et al.*, 2006; Schmid *et al.*, 2014). In laminography, the tilted



OPEN ACCESS

geometry becomes more difficult with higher-resolution (shorter focal length) Fresnel zone plates (FZPs), with a risk of collision with upstream optical elements (Witte *et al.*, 2020). Focused ion beam milling combined with scanning electron microscopy (FIB-SEM) is also a powerful tool for observation of polymer 3D structures (Denk & Horstmann, 2004). However, all of these methods are able to achieve elemental mapping when they are further combined with spectral microscopy.

The dual-energy contrast imaging method, developed on an STXM, is performed to achieve 2D elemental mapping (Ade *et al.*, 1992; Jiang *et al.*, 2010; Smit *et al.*, 2008). In this method, the absorption of a certain element in the sample will abruptly increase when the incident X-ray energy changes from its pre-edge  $E_1$  to the absorption edge  $E_2$ , while the absorption changes of other elements are so small that they can be neglected (Warp & Dobbins, 2003; Zhang, Xu *et al.*, 2010). Hitchcock *et al.* investigated 3D chemical mappings of a polyacrylate polyelectrolyte ionomer embedded with polystyrene microspheres at multiple photon energies (Hitchcock *et al.*, 2008; Johansson *et al.*, 2007). Yao *et al.* achieved the distributions of intracellular nanomaterials in three dimensions in macrophages by combining the dual-energy contrast imaging method and equally sloped tomography (Yao *et al.*, 2018). This combined approach, however, needs image alignment and refocusing during each tomography rotation and therefore is more time-consuming for data acquisition at multiple energies.

Focal stacks (FS) imaging is an emerging three-dimensional reconstruction method extended towards STXM, making possible for of the order of hundreds of nanometres reconstruction of test samples in about an hour, thus providing a flexible and fast solution for 3D imaging (Streibl, 1985; Jochum, 1988). A series of 2D microscopic images are collected by moving a sample along the optical axis with a fixed step without rotation. After processing the nanoscale 2D image sequences with the improved variance-based FS algorithm we proposed, a 3D structured image can be quickly reconstructed (Ma *et al.*, 2019). In previous work, we reconstructed the 3D image of a 4  $\mu\text{m}$ -thick cellulose film embedded with  $\text{Fe}_3\text{O}_4$  nanoparticles within about 66 min (Ma *et al.*, 2019).

In this communication, we report the 3D dual-energy FS imaging method, which exploits the combination of FS imaging and the dual-energy contrast method to quickly generate 3D elemental mapping on the nanoscale. Firstly, a simulation experiment was

conducted to validate the feasibility of the method. It was further carried out to achieve the element spatial mapping in composite nanofibers. For the first time, the 3D dual-energy FS imaging method can be used to reconstruct porous polystyrene (PS) doped with  $\text{Fe}(\text{acac})_3$ .

## 2. Experimental setup and method

The experimental setup of STXM, shown in Fig. 1(a), is used for dual-energy FS imaging, which enables microscopic images based on density, element and different contrast of samples to be acquired. A schematic of the 3D dual-energy FS imaging method is shown in Fig. 1(b). Before discussions on the 3D reconstruction, we analyze a line scan taken along an edge of the sample in the STXM image to obtain the near-edge X-ray absorption fine-structure spectroscopy (NEXAFS) spectra of the element, as well as the energies  $E_1$  and  $E_2$  (Ohmer *et al.*, 2015; Nilsson *et al.*, 2005). Two series of 2D image sequences are collected at  $E_1$  and  $E_2$ , respectively. Next, we exploit the 3D FS algorithm to reconstruct 3D structure images under the two energy edges (Ma *et al.*, 2019). The dual-energy ratio-contrast algorithm or  $K$ -edge subtraction algorithm is finally performed to elucidate detailed spatial distributions of the element of interest in the sample, so 3D mappings of the element can be seen clearly.

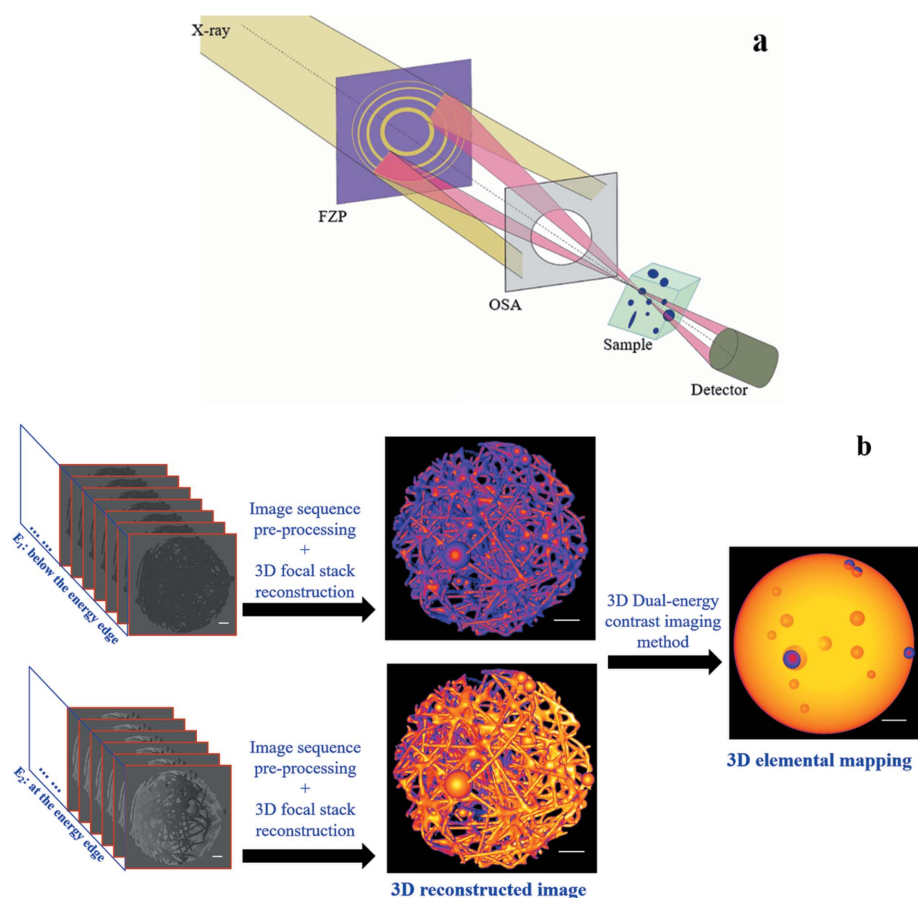


**Figure 1**

(a) Experiment setup for scanning transmission soft X-ray microscopy. (b) Schematic layout of the 3D dual-energy focal stacks (FS) reconstruction method. Scale bar: 500 nm.

### 3. Simulation

We conducted a dual-energy FS simulation of a modeled sample – a carbon cube randomly embedded with iron (Fe) and manganese (Mn) nanoparticles, ranging from 100 to 600 nm [Fig. 2(a)]. In the simulation, incident photon energies were 708 eV and 700 eV at the Fe  $L_3$  energy edge and pre-edge, respectively. The FZP has a diameter of 60  $\mu\text{m}$ , a central-stop-radius of 24  $\mu\text{m}$  and an outermost zone width ( $\Delta r_n$ ) of 10 nm, so the depth of focus (DOF) was calculated to be about 230 nm. Fresnel–Kirchhoff diffraction and X-ray multi-slice propagation theories were used for acquisition of the STXM images (Goodman, 2005; Attwood, 2017; Maiden *et al.*, 2012; Ma *et al.*, 2019). Figs. 2(b)–2(c) show two examples of images of size 3  $\mu\text{m} \times 3 \mu\text{m}$  collected at  $E = 708$  eV and 700 eV. Note that the signal from Fe particles at 700 eV has been ignored since there is too much absorption change to be detected as can be seen in Fig. 2(c).

Then, the sample was moved along the optical axis with a step of 50 nm to sequentially collect 61 images at 708 eV and 700 eV. Finally, 3D reconstructions at the two energy edges were computed by the improved FS algorithm. Fig. 2(d) shows a 3D image reconstructed at 708 eV, in which Fe and Mn particles are clearly seen; however, they are indistinguishable in the sample. Similarly, a 3D map at 700 eV with FS analysis is shown in Fig. 2(e). Fig. 2(f) presents two different renderings in a combined map of the reconstructed image from 700 eV and Fe nanoparticles from the dual-energy FS image, in which

the distributions of the reconstructed structures are in agreement with that in the modeled sample. Due to the effect of color superposition, there is a slight color difference between Mn and the corresponding gray colormap. The method was further introduced to composite nanofibers to explore its 3D characterization applications in real samples.

### 4. Experiment

An imaging experiment on composite nanofibers was carried out at the PolLux beamline station, Swiss Light Source (Raabe *et al.*, 2008). The porous-structured Fe(acac)<sub>3</sub> PS nanofibers [PS@Fe(acac)<sub>3</sub>] were produced by soaking pure PS nanofibers in a 10 wt% Fe(acac)<sub>3</sub> ethanol solution overnight. Experimentally, the 2D dual-energy contrast imaging method was firstly performed to explore 2D distributions of Fe(acac)<sub>3</sub> in the composite fibers. Two STXM images acquired at the 705 eV and 712 eV energy edges are shown in Figs. 3(a) and 3(b), respectively (NEXAFS spectra are shown in Fig. S1 of the supporting information). By analysis using the dual-energy ratio-contrast algorithm, the result shows 2D distributions and accumulation of Fe(acac)<sub>3</sub>, Fig. 3(c). According to the colorbar on the right, red represents high density of the sample, blue corresponds to low density, and dark blue means zero density. Close examination of the dual-energy contrast image, as indicated by the yellow arrows, shows there are cases where there appears to be accumulations of Fe(acac)<sub>3</sub> parti-

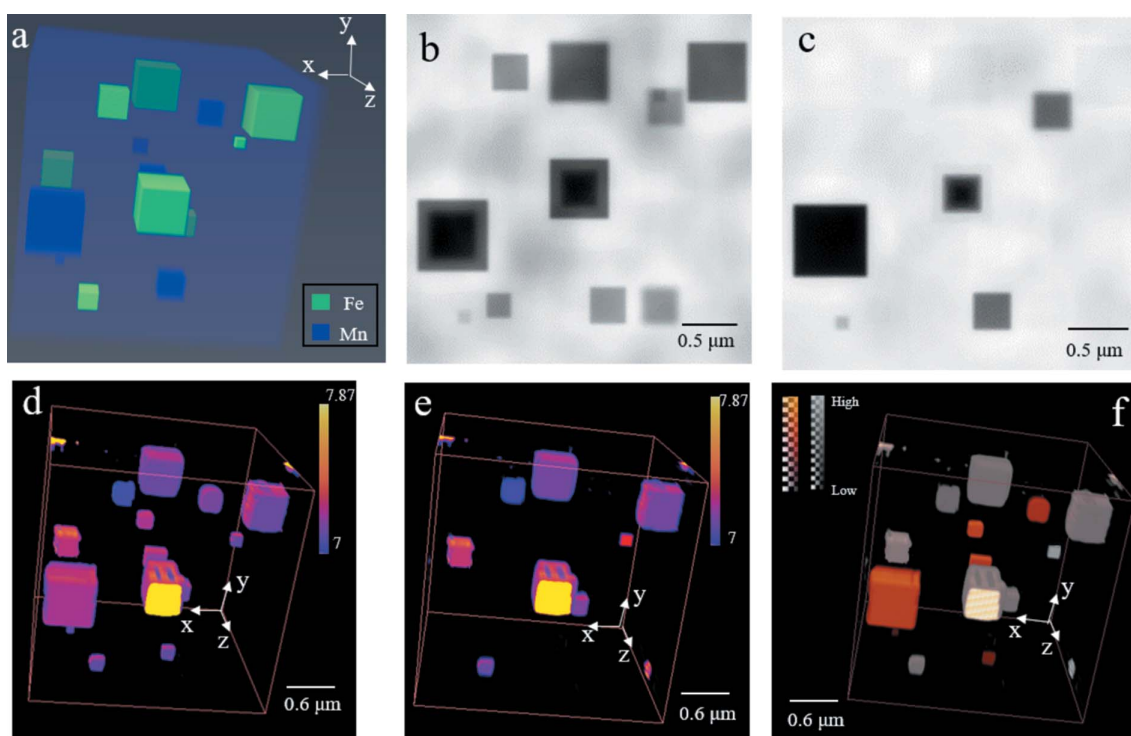


**Figure 2**

Simulation study with a modeled sample using the 3D dual-energy focal stacks imaging method. (a) The sample model in the simulation. The iron (Fe) and manganese (Mn) cubic particles are randomly distributed inside the carbon matrix sample with sizes of 100 to 600 nm. The green color represents Fe particles and blue cubes represent Mn. (b, c) 2D STXM images acquired at  $E = 708$  eV and  $E = 700$  eV, respectively. (d, e) 3D reconstructed images of the sample at 708 eV and 700 eV. The colorbar to the right represents the sample density, which is proportional to the optical density. Unit of colorbar:  $\text{g cm}^{-3}$ . (f) 3D combined representations of Fe (gray color) and Mn (orange color) distributions.

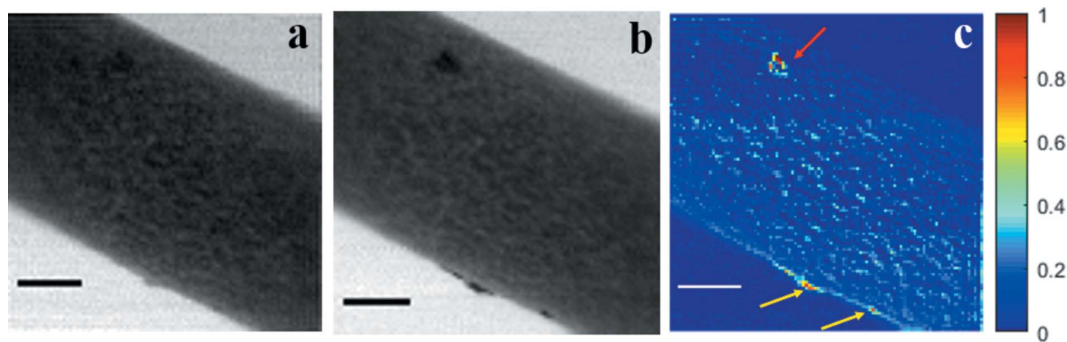


**Figure 3** Soft X-ray STXM images and the dual-energy contrast images for the PS@Fe(acac)<sub>3</sub> composite nanofibers. (a, b) STXM images collected at  $E_1 = 705$  eV and  $E_2 = 712$  eV, respectively. (c) 2D dual-energy contrast image from analysis of (a) and (b). The scale bar is 1  $\mu\text{m}$ .

cles on the sides of fibers. However, it is insufficient, as the red arrow indicates, to distinguish the positions of Fe(acac)<sub>3</sub> from the 2D structured image.

To quickly distinguish the spatial distribution of Fe(acac)<sub>3</sub> in the porous composite nanofibers, a 3D dual-energy FS experiment was carried out based on STXM for Fe(acac)<sub>3</sub> spatial localization. In the experiment,  $\Delta r_n$  of the FZP was 15 nm so the DOF was about 500 nm. Taking into account the DOF and oversampling, the step size of the motor along the optical axis was set as 300 nm. By moving the sample with a fixed step, 40 images were collected sequentially over 12  $\mu\text{m}$  along the optical axis to ensure each part of the structure was within the DOF in one of the 2D micrographs at 712 eV, as well as at 705 eV. The automatic image acquisition for FS experimental study was about 3 h without any extra operation or particular sample preparation, which is evidently faster than STXM-based nanotomography under the similar resolution condition. The 3D FS reconstructions were computed using the improved variance-based FS algorithm after image pre-processing of normalization, denoising, and image sequences alignment (Ma *et al.*, 2019). The result shown in Fig. 4(a) is a 3D map of PS@Fe(acac)<sub>3</sub> composite nanofibers reconstructed at 712 eV, the angle observation of which is consistent with that in Fig. 3. Colors in the image indicate the densities of fibers as shown by the fire scale colorbar in the upper right corner. Yellow means high density and blue corresponds to low density of the composite nanofiber. The 3D visualization video can be found in Movie 1 of the supporting information. In Movie 1, 3D structures of composite nanofibers are shown more clearly; however, it is impossible to differentiate the positions of Fe(acac)<sub>3</sub> in the porous fibers. It is hence desirable to combine with the dual-energy contrast imaging method.

By processing and analyzing the two 3D reconstruction images with the dual-energy ratio-contrast algorithm, spatial distributions of Fe(acac)<sub>3</sub> were obtained. Fig. 4(b) shows 3D mappings of Fe(acac)<sub>3</sub> from the same view as Fig. 4(a), in which the Fe(acac)<sub>3</sub> can be seen clearly (see Movie 2 of the supporting information). There are some accumulation and agglomerations, consistent with the SEM result in Fig. S2. Movie 2 clearly shows that the Fe(acac)<sub>3</sub> particles or large agglomerations are mostly distributed around surfaces or

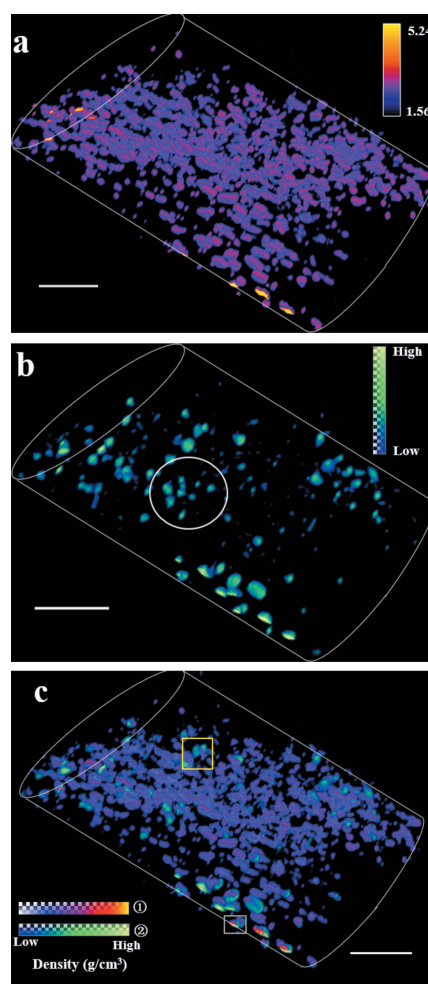


**Figure 4** 3D reconstruction of PS@Fe(acac)<sub>3</sub> composite nanofibers and the spatial distribution of Fe(acac)<sub>3</sub>. (a) 3D reconstruction of PS@Fe(acac)<sub>3</sub> composite nanofibers. The colorbar to the right indicates the sample density. The larger the value, the higher the density value, and it is proportional to the optical density. Color scale is in  $\text{g cm}^{-3}$ . (b) Spatial distributions of Fe(acac)<sub>3</sub> after dual-energy FS reconstruction from the same angle observation of (a). (c) Volume rendering of the nanofibers and distributions of Fe(acac)<sub>3</sub> simultaneously. The ‘Temperature’ colormap represents the fibers reconstructed from  $E = 705$  eV [legend (1)] and the ‘VolrenGreen’ colormap shows the Fe(acac)<sub>3</sub> mapping [legend (2)]. Panel (c) is in the same rotation view as (a) and (b). Gray and yellow boxes are two obvious examples showing Fe(acac)<sub>3</sub> inside the fibers. Scale bar: 1  $\mu\text{m}$ .

edges of the fibers, the accumulation of which is relatively less than that on the surface. For example, the Fe(acac)<sub>3</sub> particles marked by a white dotted circle in Fig. 4(b) are actually inside the nanofibers shown in Movie 2. Furthermore, we observed nanostructures of fibers and Fe(acac)<sub>3</sub> distributions simultaneously with a two-colormap combination [Fig. 4(c)]. The presentation was made by combining the 3D reconstruction image at 705 eV and spatial Fe(acac)<sub>3</sub> mapping. It is clear that the distributions of Fe(acac)<sub>3</sub> in the nanofibers are varied. Taking two details as examples, nanoparticles in the gray box in Fig. 4(c) show the Fe(acac)<sub>3</sub> inside the fiber. Similarly, the yellow marked parts are also inside the fibers. In addition, the dose used to acquire this image sequence at 712 eV was only  $\sim 7.2 \times 10^5$  Gy (supporting information), which is typically lower than the corresponding full-field imaging or nanotomography (typical  $10^6$  to  $10^8$  Gy) (Gros *et al.*, 2005; Meyer-Ilse *et al.*, 2001). Thus, radiation damage is a considerable advantage by STXM compared with full-field microscopy.

## 5. Conclusion

In conclusion, we have developed the three-dimensional dual-energy FS method for fast elemental mappings in a sample. The spatial elemental distribution is directly reconstructed from two series of image sequences using the improved variance-based focal stack algorithm and dual-energy ratio-contrast algorithm. Both simulation and applicable experimental results have indicated the feasibility of the 3D imaging method. Reconstructed Fe(acac)<sub>3</sub> particles were randomly distributed inside the porous composite nanofibers or on the surface. Compared with conventional nanotomography, the 3D dual-energy FS imaging method reduces by more than two-thirds of the time to achieve a similar resolution result. Thus, the advantages of the 3D dual-energy FS method are its quick, efficient and quantitative elementally reconstruction at nanoscale resolution, as well as no extra and particular sample preparation or labeling. It is expected that the 3D dual-energy FS method will offer broader characterization applications in nanomedicine, biological and other fields.

## Acknowledgements

The authors thank PolLux beamline of Swiss Light Source and BL08U1A beamline of Shanghai Synchrotron Radiation Facility for providing beam time. They also thank Katharina Witte (Swiss Light Source, Paul Scherrer Institute) for assisting with the data acquisition.

## Funding information

This work was supported by the National Natural Science Foundation of China (Nos. 51773221, 11875316 and U1832146) and the Youth Innovation Promotion Association CAS (Nos. 2017308 and 2019291).

## References

Ade, H., Zhang, H., Cameron, S., Costello, C., Kirz, J. & Williams, S. (1992). *Science*, **258**, 972–975.

Attwood, D. (2017). *Soft X-rays and Extreme Ultraviolet Radiation: Principles and Applications*. Cambridge University Press.

Denk, W. & Horstmann, H. (2004). *PLoS Biol.* **2**, e329.

González del Campo, M. M., Darder, M., Aranda, P., Akkari, M., Huttel, Y., Mayoral, A., Bettini, J. & Ruiz-Hitzky, E. (2018). *Adv. Funct. Mater.* **28**, 1703048.

Goodman, J. W. (2005). *Introduction to Fourier Optics*. McGraw-Hill.

Hitchcock, A. P., Johansson, G. A., Mitchell, G. E., Keefe, M. H. & Tyliszczak, T. (2008). *Appl. Phys. A*, **92**, 447–452.

Jiang, H., Song, C., Chen, C. C., Xu, R., Raines, K. S., Fahimian, B. P., Lu, C. H., Lee, T. K., Nakashima, A., Urano, J., Ishikawa, T., Tamanoi, F. & Miao, J. (2010). *Proc. Natl Acad. Sci. USA*, **107**, 11234–11239.

Jo, M. S., Park, G. D., Kang, Y. C. & Cho, J. S. (2018). *Nanoscale*, **10**, 13539–13547.

Jochum, L. (1988). *X-ray Microscopy II*, Vol. 56 of *Springer Series in Optical Science*, pp. 292–295 Springer.

Johansson, G. A., Dynes, J. J., Hitchcock, A. P., Tyliszczak, T., Swerhone, G. D. & Lawrence, J. R. (2006). *Microsc. Microanal.* **12**, 1412–1413.

Johansson, G. A., Tyliszczak, T., Mitchell, G. E., Keefe, M. H. & Hitchcock, A. P. (2007). *J. Synchrotron Rad.* **14**, 395–402.

Le Gros, M. A., McDermott, G. & Larabell, C. A. (2005). *Curr. Opin. Struct. Biol.* **15**, 593–600.

Lin, J., Ding, B., Yang, J., Yu, J. & Sun, G. (2012). *Nanoscale*, **4**, 176–182.

Lin, J., Shang, Y., Ding, B., Yang, J., Yu, J. & Al-Deyab, S. S. (2012). *Mar. Pollut. Bull.* **64**, 347–352.

Ma, L. M., Zhang, X. Z., Xu, Z. J., Späth, A., Xing, Z. J., Sun, T. X. & Tai, R. Z. (2019). *Opt. Express*, **27**, 7787–7802.

Mahapatra, A., Mishra, B. G. & Hota, G. (2013). *J. Hazard. Mater.* **258–259**, 116–123.

Maiden, A. M., Humphry, M. J. & Rodenburg, J. M. (2012). *J. Opt. Soc. Am. A*, **29**, 1606–1614.

McIntosh, R., Nicastrò, D. & Mastronarde, D. (2005). *Trends Cell Biol.* **15**, 43–51.

Meyer-Ilse, W., Hamamoto, D., Nair, A., Lelièvre, S. A., Denbeaux, G., Johnson, L., Pearson, A. L., Yager, D., Legros, M. A. & Larabell, C. A. (2001). *J. Microsc.* **201**, 395–403.

Miyamoto, A., Lee, S., Cooray, N. F., Lee, S., Mori, M., Matsuhisa, N., Jin, H., Yoda, L., Yokota, T., Itoh, A., Sekino, M., Kawasaki, H., Ebihara, T., Amagai, M. & Someya, T. (2017). *Nat. Nanotechnol.* **12**, 907–913.

Moatmed, S. M., Khedr, M. H., El-dek, S. I., Kim, H.-Y. & El-Deen, A. G. (2019). *J. Environ. Chem. Eng.* **7**, 103508.

Nilsson, H. J., Tyliszczak, T., Wilson, R. E., Werme, L. & Shuh, D. K. (2005). *Anal. Bioanal. Chem.* **383**, 41–47.

Ohmer, N., Fenk, B., Samuelis, D., Chen, C. C., Maier, J., Weigand, M., Goering, E. & Schütz, G. (2015). *Nat. Commun.* **6**, 6045.

Raabe, J., Tzvetkov, G., Flechsig, U., Böge, M., Jaggi, A., Sarafimov, B., Vernooij, M. G. C., Huthwelker, T., Ade, H., Kilcoyne, D., Tyliszczak, T., Fink, R. H. & Quitmann, C. (2008). *Rev. Sci. Instrum.* **79**, 113704.

Schmid, G., Zeitvogel, F., Hao, L., Ingino, P., Kuerner, W., Dynes, J. J., Karunakaran, C., Wang, J., Lu, Y., Ayers, T., Schietinger, C., Hitchcock, A. P. & Obst, M. (2014). *Microsc. Microanal.* **20**, 531–536.

Shenhar, R. & Rotello, V. M. (2003). *Acc. Chem. Res.* **36**, 549–561.

Smit, E. de, Swart, I., Creemer, J. F., Hoveling, G. H., Gilles, M. K., Tyliszczak, T., Kooyman, P. J., Zandbergen, H. W., Morin, C., Weckhuysen, B. M. & de Groot, F. M. F. (2008). *Nature*, **456**, 222–225.

Streibl, N. (1985). *J. Opt. Soc. Am. A*, **2**, 121–127.

Warp, R. J. & Dobbins, J. T. (2003). *Med. Phys.* **30**, 190–198.

Wei, M., Wan, J., Hu, Z., Peng, Z., Wang, B. & Wang, H. (2017). *Appl. Surf. Sci.* **391**, 267–274.

- Witte, K., Späth, A., Finizio, S., Donnelly, C., Watts, B., Sarafimov, B., Odstřil, M., Guizar-Sicairos, M., Holler, M., Fink, R. H. & Raabe, J. (2020). *Nano Lett.* **20**, 1305–1314.
- Yao, S., Fan, J., Chen, Z., Zong, Y., Zhang, J., Sun, Z., Zhang, L., Tai, R., Liu, Z., Chen, C. & Jiang, H. (2018). *IUCrJ*, **5**, 141–149.
- Zhang, H., Han, J. S. & Yang, B. (2010). *Adv. Funct. Mater.* **20**, 1533–1550.
- Zhang, X. Z., Xu, Z. J., Tai, R. Z., Zhen, X. J., Wang, Y., Guo, Z., Yan, R., Chang, R., Wang, B., Li, M., Zhao, J. & Gao, F. (2010). *J. Synchrotron Rad.* **17**, 804–809.